International Journal of Solids and Structures 51 (2014) 1–12

Contents lists available at ScienceDirect

International Journal of Solids and Structures

journal homepage: www.elsevier.com/locate/ijsolstr

Dynamic stability of externally pressurized elastic rings subjected to high rates of loading

Thibaut Putelat [a], Nicolas Triantafyllidis [a,b,c,*]

[a] Laboratoire de Mécanique des Solides, UMR CNRS 7649, Ecole Polytechnique, 91128 Palaiseau Cedex, France
[b] Département de Mécanique, École Polytechnique, 91128 Palaiseau Cedex, France
[c] Aerospace Engineering Department & Mechanical Engineering Department (emeritus), The University of Michigan, Ann Arbor, MI 48109-2140, USA

ARTICLE INFO

Article history:
Received 29 January 2013
Received in revised form 29 July 2013
Available online 19 August 2013

Keywords:
Stability
Elastic wave
Nonlinear dynamics
Localization of deformation

ABSTRACT

Of interest here is the influence of loading rate on the stability of structures where inertia is taken into account, with particular attention to the comparison between static and dynamic buckling. This work shows the importance of studying stability via perturbations of the initial conditions, since a finite velocity governs the propagation of disturbances. The method of modal analysis that determines the fastest growing wavelength, currently used in the literature to analyze dynamic stability problems, is meaningful only for cases where the velocity of the perfect structure is significantly lower than the associated wave propagation speeds.

As a model structure to illustrate this point we select an elastic ring subjected to external hydrostatic pressure which is applied at different rates ϵ (appropriately non-dimensionalized with respect to elastic axial wave speed). The ring's stability is studied by following the evolution of a localized small perturbation. It is shown that for small values of the applied loading rate, the structure fails through a global mode, while for large values of the applied loading rate the structure fails by a localized mode of deformation. An analytically obtained localization time t_l is found to be a very good estimate of the onset of instability time at high loading rates.

1. Introduction

The issue of dynamic stability of structures is an important engineering problem and as such has drawn considerable attention. The first investigation in this area appears to be the work of Koning and Taub (1933), who investigated the influence of inertia in a simply supported imperfect column subjected to a sudden axial load. A substantial amount of work followed that investigated the response of, mainly elastic, structures to impulse or time-dependent loads. As a result, and due to the many possible definitions for the stability of time-dependent systems, the term *dynamic stability* encompasses many classes of problems and different physical phenomena and has many interpretations, with inertia being the only common denominator.

In the absence of inertia, the processes of failure by a bifurcation instability mode in elastic solids and structures is well understood (e.g. Brush and Almroth, 1975) and a general asymptotic analysis, termed Lyapunov–Scmidt–Koiter (LSK), has been developed for their study. The first effort to use the LSK general analysis for the dynamic stability problem of an elastic structure appears to be Budiansky and Hutchinson (1964), where the authors proposed an asymptotic analysis of the time-dependent problem using the eigenmodes of the static problem. Alternative methods, based on upper and lower bounds of the structure's energy have also been proposed and the interested reader is referred to Chapter 12 in Simitses and Hodges (2006) for a well written account of this approach.

Another idea, popular in fluid mechanics, has also been adopted for the dynamic stability analysis of solids with more general constitutive laws under high rates of loading, according to which one seeks the solid's fastest growing eigenmode. This type of analysis is also termed the *method of frozen coefficients*, since the resulting PDE system of the linearized stability equations become autonomous by virtue of ignoring the time-independence of their coefficients. This method has been repeatedly applied in the study of dynamic stability of elastoplastic bars and rings under high loading rates where the size of fragments is of interest (e.g. see Shenoy and Freund, 1999; Sorensen and Freund, 2000; Mercier and Molinari, 2003). However, recent experimental evidence from rapidly expanding electromagnetically loaded metallic rings by Zhang and Ravi-Chandar (2006, 2008) finds no evidence of a dominant wavelength at the necked pattern of the rings. As explained by

* Corresponding author. Address: Laboratoire de Mécanique des Solides, UMR CNRS 7649, France. Tel.: +33 1 69 33 57 98.
E-mail addresses: putelat@lms.polytechnique.fr (T. Putelat), nick@lms.polytechnique.fr (N. Triantafyllidis).

0020-7683/$ - see front matter © 2013 Elsevier Ltd. All rights reserved.
http://dx.doi.org/10.1016/j.ijsolstr.2013.08.002

these authors, using the fastest growing eigenmode to predict the onset of failure is physically meaningful provided that the loading rate is much slower than the speed of propagation of perturbations in the solid or structure at hand. For high loading rates, commensurate with some characteristic wave propagation speed in the structure, a novel approach to the stability analysis is required, namely the study of evolution of localized perturbations.

In contrast to the above mentioned cases of structures under rapid extension, of particular interest in this work is the influence of loading rate on the stability of structures under compression that exhibit an instability even under quasistatic loading. As a model structure to illustrate these ideas, we select an elastic ring subjected to external hydrostatic pressure which is applied at different rates ϵ (appropriately non-dimensionalized with respect to elastic axial wave speed). Of course such a classical topic has been treated repeatedly in the mechanics literature; following the work of Carrier (1945), different linear and nonlinear versions of the ring dynamical equations of increasing complexity have been proposed (e.g. Morley, 1961; Goodier and McIvor, 1964; Boresi and Reichenbach, 1967; Wah, 1970; Graff, 1971; Simmonds, 1979; Dempsey, 1996) to study their vibrations. The stability of rings subjected to impulsive or step loadings has also been repeatedly studied (e.g. Goodier and McIvor, 1964; Lindberg, 1964; Florence, 1968; Anderson and Lindberg, 1968a; Lindberg, 1974; Simmonds, 1979; Lindberg and Florence, 1987; Amabili and Paidoussis, 2003). These studies rely on modal analysis using Fourier series whose truncation leads nonlinear amplitude equations and showed that dynamic buckling is triggered by flexural modes. At leading order, the dynamics of flexural modes are governed by Mathieu-Hill equations whose characteristic curves of associated Mathieu functions delineate boundaries of instability domains within the control parameter plane of load versus ring's slenderness. For an account of dynamic stability problems in rings, the interested reader is referred to the book Graff (1975) and references quoted therein.

All the above-mentioned works were concerned with the stability of ring vibrations and not with their stability at high loading rates as is the case of interest here. Our investigation is further motivated by work involving rings high strain-rate using electromagnetic loading – since this method avoids propagating waves – under tension (Gourdin, 1989; Triantafyllidis and Waldenmyer, 2004; Zhang and Ravi-Chandar (2006); Zhang and Ravi-Chandar (2008)) that study the influence of high loading rate on metal ductility and in particular by experiments in ring and cylinder under electromagnetic compression by Anderson and Lindberg (1968b) and Jones and Okawa (1976), since these experiments combine structural instability with rapid loading. It is the most recent experimental work of Mainy (2012) that serves as the starting point for this investigation, and in particular the localized failure patterns observed (see Fig. 1), which are in marked contrast with global buckling modes of externally pressurized rings under quasistatic loading rates. In order to keep essential features such as buckling under static loading and finite wave speeds for all wavenumbers, we concentrate on the dynamics of an elastic ring following a von Karman – Timoshenko theory allowing for small strains, moderate rotations, transverse shear and rotational inertia. The ring's stability is studied by following the evolution of a localized small perturbation. It is shown that for small values of the applied loading rate the structure fails through a global mode, while for large values of the applied loading rate the structure fails by a localized mode of deformation. Following Section 1 the presentation of the work continues with Section 2, where we derive the equations of motion and outline the numerical scheme for the solution of these equations. The results are given in Section 3 where we present the linearized analysis of the initial growth/decay of a perturbation followed by numerical calculations of the evolution of a spatially localized displacement perturbation and a discussion in Section 4 concludes this work.

2. Formulation

In the first subsection we derive the equations of motion from Hamilton's variational principle, from which we deduce the structure's Euler–Lagrange equations. The numerical scheme for the solution of these equations is outlined in the second subsection.

2.1. Equations of motion

We consider a homogeneous linear elastic ring of rectangular section with thickness h, width a and cross sectional area $A = h \times a$. The ring has a mid-line radius r and follows small strain – moderate rotation Timoshenko kinematics described by $\tilde{v}(\theta), \tilde{w}(\theta), \tilde{\psi}(\theta)$ respectively the tangential and normal displacements of the ring's reference mid-line at point θ and the rotation of the section perpendicular to the mid-line, initially at θ (see Fig. 1).

To find the system's Lagrangian, we need to determine its potential and kinetic energies $\mathcal{P}$ and $\mathcal{K}$ respectively. The potential energy $\mathcal{P}$ consists of two parts: the stored elastic energy $\mathcal{P}_{\text{int}}$ plus $\mathcal{P}_{\text{ext}}$ the work potential of the externally applied uniform pressure $\tilde{\lambda}$, namely

$$\mathcal{P} = \mathcal{P}_{\text{int}} + \mathcal{P}_{\text{ext}}. \tag{1}$$

The stored elastic energy $\mathcal{P}_{\text{int}}$ is

$$\mathcal{P}_{\text{int}} = \int_0^{2\pi} \left\{ \int_{-h/2}^{h/2} \left(E\varepsilon_{\theta\theta}^2 + G\gamma_{r\theta}^2\right) dz \right\} a\, r\, d\theta, \tag{2}$$

where the axial and shear strains $\varepsilon_{\theta\theta}$ and $\gamma_{r\theta}$ are given by

$$\varepsilon_{\theta\theta} = \frac{\tilde{v}' + \tilde{w}}{r} + \frac{1}{2}\left(\frac{\tilde{v} - \tilde{w}'}{r}\right)^2 + z\frac{\tilde{\psi}'}{r}, \quad \gamma_{r\theta} = \frac{\tilde{v} - \tilde{w}'}{r} - \tilde{\psi}, \tag{3}$$

with $f' \equiv \partial f/\partial\theta$ denoting the θ-derivative of the corresponding function and E, G the material's Young and shear moduli, respectively.

The kinematic and stress state assumptions leading to (2) and (3) are that cross-sections perpendicular to the initial middle line deform as planes, the ring is in the state of an approximate uniaxial stress $\sigma_{\theta\theta} = E\varepsilon_{\theta\theta}$, strains are small but rotations are moderate and that shear stress $\sigma_{r\theta} = G\gamma_{r\theta}$ although negligible compared to $\sigma_{\theta\theta}$ does contribute to the ring's elastic energy.

By inserting (3) into (2) and integrating through the thickness, the following expression is obtained for the internal energy

$$\mathcal{P}_{\text{int}} = \frac{1}{2}\int_0^{2\pi} \left\{ EA\left[\frac{\tilde{v}' + \tilde{w}}{r} + \frac{1}{2}\left(\frac{\tilde{v} - \tilde{w}}{r}\right)^2\right]^2 + EI\left(\frac{\tilde{\psi}'}{r}\right)^2 + \chi G\left(\frac{\tilde{v} - \tilde{w}'}{r} - \tilde{\psi}\right)^2 \right\} r d\theta, \tag{4}$$

where $I = ah^3/12$ is the cross sectional moment of inertia and χ the shear correction factor ($\chi = 2/3$ for a rectangular section, the energy expression in (4) being valid for arbitrary cross sections with appropriate A and I expressions). For the thin rings of interest here, it is tacitly assumed that the radius of the mid-line $r \gg h$.

The work potential $\mathcal{P}_{\text{ext}}$ of the external pressure loading $\tilde{\lambda}$ applied on the ring equals $\tilde{\lambda}\Delta S$ where ΔS is the change of area due to deformation $(\tilde{v}, \tilde{w})$ enclosed by the ring's mid-line, which is given by e.g. Brush and Almroth (1975)

$$\mathcal{P}_{\text{ext}} = \tilde{\lambda}\int_0^{2\pi} \left[\tilde{w} + \frac{1}{2r}\left(\tilde{v}^2 - \tilde{v}\tilde{w}' + \tilde{v}'\tilde{w} + \tilde{w}^2\right)\right] r d\theta, \tag{5}$$

where $\tilde{\lambda}$ is taken positive when acting inwards (resulting in compressive hoop stresses $\sigma_{\theta\theta} < 0$) in the ring.

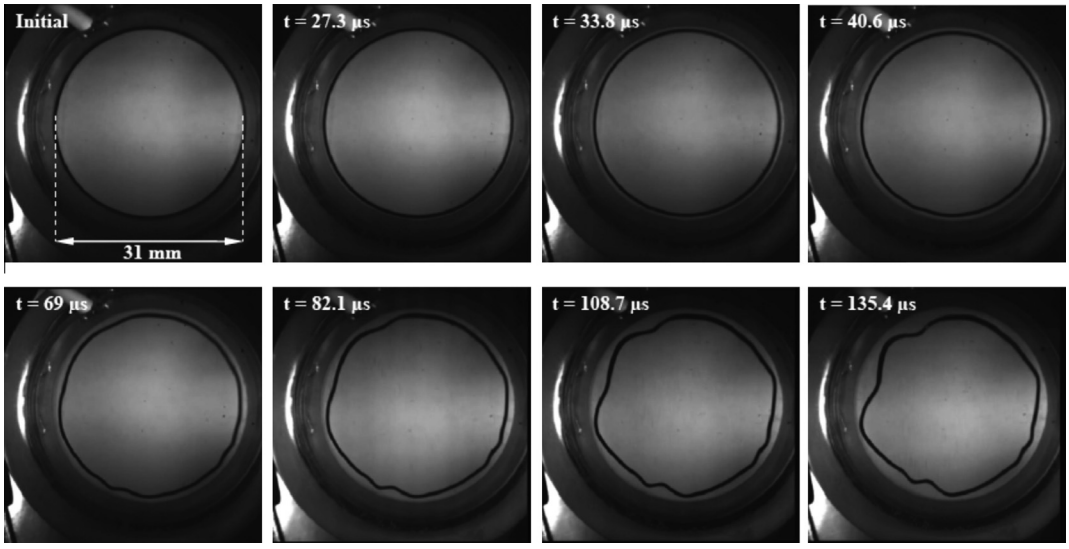

Fig. 1. Sequence of images of electromagnetically compressed Al rings by Mainy (2012). Courtesy of Prof. K. Ravi-Chandar, University of Texas Austin.

Using the same kinematic assumptions as for the derivation of (3), the tangential $\dot{\tilde{v}}_\theta$ and radial $\dot{\tilde{v}}_r$ velocities of an arbitrary material point on the ring are

$$\dot{\tilde{v}}_\theta = \dot{\tilde{v}} + z\dot{\tilde{\psi}}, \quad \dot{\tilde{v}}_r = \dot{\tilde{w}} \tag{6}$$

where $\dot{f} \equiv \partial f/\partial \tilde{t}$ denotes time-differentiation of the corresponding function. Consequently the kinetic energy of the ring is

$$\mathcal{K} = \frac{1}{2}\int_0^{2\pi}\left\{\int_{-h/2}^{h/2}\rho\left(\dot{\tilde{v}}_\theta^2 + \dot{\tilde{v}}_r^2\right)dz\right\} a\, r\, d\theta, \tag{7}$$

where ρ is the mass density of the ring. Using (6) into (7) and again recalling that $r \gg h$ when integrating through the thickness, we obtain for the kinetic energy

$$\mathcal{K} = \frac{1}{2}\int_0^{2\pi}\rho\left[A\left(\dot{\tilde{v}}^2 + \dot{\tilde{w}}^2\right) + I\dot{\tilde{\psi}}^2\right] r\, d\theta. \tag{8}$$

The system's Lagrangian is now determined by

$$\mathcal{L} = \mathcal{K} - \mathcal{P} = \mathcal{K} - (\mathcal{P}_{\text{int}} + \mathcal{P}_{\text{ext}}). \tag{9}$$

Before proceeding to the application of Hamilton's principle to derive the system's Euler–Lagrange equations, we find it useful to introduce some dimensionless variables and physically relevant parameters. Length, time, and stress are non-dimensionalized by $r, r/c$ and E where $c = \sqrt{E/\rho}$ is the ring's axial wave speed. Consequently the Lagrangian is a function of the dimensionless displacements and section rotation $v \equiv \tilde{v}/r, w \equiv \tilde{w}/r, \psi \equiv \tilde{\psi}/r$ while time-differentiation is now with respect to the dimensionless time $t \equiv \tilde{t}/(r/c)$. In addition, we define the slenderness parameter η, the shear factor μ and the dimensionless pressure λ as follows

$$\eta \equiv I/(Ar^2) = (h/r)^2/12; \quad \mu \equiv \chi G/E = 0.5\chi/(1+\nu);$$
$$\lambda \equiv \tilde{\lambda} r a/(EA) = (\tilde{\lambda}/E)(r/h). \tag{10}$$

As a result, from (4), (5), (8), (9), (10) and using also the definitions

$$e \equiv v' + w, \quad \phi \equiv v - w' \tag{11}$$

for the dimensionless axial strain and rotation of the ring's middleline, we obtain for the dimensionless potential and kinetic energies, also denoted $\mathcal{P}$ and $\mathcal{K}$ by abuse of notation,

$$\mathcal{P} = \int_0^{2\pi} P\, d\theta, \quad P \equiv \left[(e+\phi^2/2)^2 + \eta(\psi')^2 + \mu(\phi-\psi)^2\right]/2 + \lambda[w + (v\phi + we)/2], \tag{12}$$

$$\mathcal{K} = \int_0^{2\pi} K\, d\theta, \quad K \equiv \left[\dot{v}^2 + \dot{w}^2 + \eta\dot{\psi}^2\right]/2. \tag{13}$$

We denote P and K the system's potential and kinetic energy densities.

Using now Hamilton's principle, i.e. by extremizing the action integral $\int_0^T \mathcal{L}\, dt$ over time paths with fixed initial and final time values of the independent variables v, w and ψ, we deduce the following Euler–Lagrange equations governing respectively the axial, normal and rotational motion of the ring

$$\begin{cases} \ddot{v} = v'' - (\mu+\lambda)v + (1+\mu+\lambda)w' + \mu\psi + (\phi^2)'/2 - e\phi - \phi^3/2, \\ \ddot{w} = -\lambda - (1+\mu+\lambda)v' + \mu w'' - (1+\lambda)w + \mu\psi' - \phi^2/2 - (e\phi)' - (\phi^3)'/2, \\ \ddot{\psi} = \psi'' - (\mu/\eta)(\psi - v + w'). \end{cases} \tag{14}$$

To the above equations initial conditions for v, w, ψ and $\dot{v}, \dot{w}, \dot{\psi}$ must be added.

Of particular interest here now is the perfect structure's principal solution (v_0, w_0, ψ_0), i.e. the response of the perfect ring to a uniform pressure loading at constant rate ϵ (starting at $t = 0$): $\lambda = \epsilon t$. Due to axisymmetry of the structure and loading $v_0(\theta, t) = \psi_0(\theta, t) = 0$ while $w_0(\theta, t) = w_0(t)$ is according to $(14)_2$

$$\ddot{w}_0 + (1 + \epsilon t)w_0 + \epsilon t = 0, \tag{15}$$

with initial conditions $w_0(0) = \dot{w}_0(0) = 0$. For pressure levels corresponding to small deformations $w_0(t)$, i.e. such that $\epsilon t \ll 1$, an asymptotic solution makes sense for a bounded time domain. To this end we consider the following expansion for $w_0(t)$

$$w_0(t) = \epsilon w_1(t) + \epsilon^2 w_2(t) + \epsilon^3 w_3(t) + \cdots \tag{16}$$

Introducing (16) into (15) and collecting terms of the like order ϵ leads to the following recursive system

$$\ddot{w}_1 + w_1 + t = 0 \quad \text{at } O(1), \quad \ddot{w}_n + w_n + t w_{n-1} = 0 \quad \text{at } O(n). \tag{17}$$

Solution of the above system, after taking into account the initial conditions $w_0(0) = \dot{w}_0(0) = 0$ yields, up to $O(\epsilon^3)$

$$w_1(t) = \sin t - t \tag{18}$$

$$w_2(t) = -[t\sin(t) + (-t^2 - 8)\cos(t) - 4t^2 + 8]/4, \tag{19}$$

$$w_3(t) = -[(3t^4 + 33t^2 + 735)\sin(t) + (10t^3 + 33t)\cos(t) + 96t^3 - 768t]/96. \tag{20}$$

From (18) we see that the leading order approximation shows a dimensionless $2\pi-$periodic oscillation superimposed to a linear component for the radial displacement. In Fig. 2, we compare the exact (numerical) solution of (15) to its asymptotic approximations given by (16)–(20) up to $O(\epsilon^3)$. This shows that, over the interval $t \in [0, +\infty[$, the asymptotic expansion (16) does not converge uniformly due the presence of terms which produce oscillations of increasing amplitude. Notice from Fig. 2 that the time interval of convergence improves when the order of the expansion is increased. Although improved estimates for the principal solution could be provided (e.g. based on multiscale asymptotic expansions) the analytic leading order approximation of the principal solution presented here is useful for finding the characteristic times for the problem discussed next.

2.2. Numerical method

Solving the system's governing equations in (14) is based on a numerical technique that uses the system's Hamiltonian. To this end, since the Lagrangian density of the system $L \equiv K - P$ in (13) depends on the generalized coordinates (v, w, ψ) and their derivatives $(\dot v, \dot w, \dot\psi)$, we can compute the generalized momenta p_v, p_w, p_ψ associated to (v, w, ψ) and hence the Hamiltonian density H by

$$p_v = \frac{\partial L}{\partial \dot v},\quad p_w = \frac{\partial L}{\partial \dot w},\quad p_\psi = \frac{\partial L}{\partial \dot\psi};\quad H = p_v\dot v + p_w\dot w + p_\psi\dot\psi - L. \tag{21}$$

Consequently from (21) and (13) the system's Hamiltonian density is

$$H = (1/2)\Big\{p_v^2 + p_w^2 + p_\psi^2/\eta + (e + \phi^2/2)^2 + \eta(\psi')^2 + \mu(\phi - \psi)^2 + 2\lambda[w + (v\phi + we)/2]\Big\}. \tag{22}$$

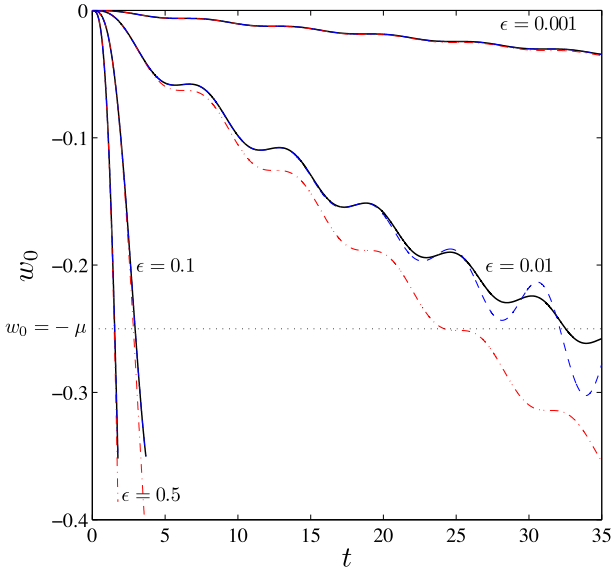

Fig. 2. Time evolution of the principal solution w_0 for several different loading rates (from slow to fast rates: $\epsilon = \{0.001, 0.01, 0.1, 0.5\}$); exact (numerical) solution and asymptotic approximations. Notation: numerical solution (thick solid line), first order asymptotic solution (18) (dotted-dashed line), third order asymptotic solution (20) (dashed line). Note the superimposed oscillations at slow loading rate.

The equations of motion are obtained in compact form from

$$\partial_t \mathbf{u} = \mathbf{J}\nabla_{\mathbf{u}} H, \tag{23}$$

where the state vector $\mathbf{u} \equiv (v, w, \psi, p_v, p_w, p_\psi)^\top$ and $\mathbf{J}$ the symplectic structure matrix.

The numerical method used for solving (23) (plus the initial condition on $\mathbf{u}$ at $t = 0$) is based on a spatial discretization of the system's Hamiltonian. Taking the first variation of the space-discretized Hamiltonian leads to a system of first order ODE's that are then solved numerically via a Runge–Kutta method. More specifically a spatial discretization is considered over a regular N-point grid in $[0, 2\pi)$ at

$$\theta_i = (i-1)\Delta\theta,\quad \Delta\theta \equiv 2\pi/N,\quad i = 1, \dots, N \tag{24}$$

resulting in the discretized Hamiltonian $\mathcal{H}_\Delta$. In calculating $\mathcal{H}_\Delta$ from its density H in (22), one needs space differentiation operators for v' and w' to calculate $v_i' = D_{ij}v_j$ and $w_i' = D_{ij}w_j$. The differentiation matrix (e.g. Weideman and Reddy, 2000; Hesthaven et al., 2007) is chosen to be, for N even,

$$D_{ij} = \begin{cases} 0 & \text{for } i = j, \\ (1/2)(-1)^{i-j}\cot[(i-j)\pi/N] & \text{for } i \neq j. \end{cases} \tag{25}$$

Taking the first variation of $\mathcal{H}_\Delta$ with respect to ith spatial degrees of freedom $\mathbf{z} \equiv \mathbf{u}(\theta_i, t)$, we finally have the $6N$-dimensional system of ODE's

$$\dot{\mathbf{z}} = (\mathbf{J}/\Delta\theta)\nabla_{\mathbf{z}}\mathcal{H}_\Delta(\mathbf{z}, t), \tag{26}$$

which is a non-autonomous system of the type $\dot{\mathbf{z}} = \mathbf{f}(t, \mathbf{z})$. This system is integrated using the following implicit midpoint scheme

$$\mathbf{z}_{n+1} = \mathbf{z}_n + \Delta t\,\mathbf{f}[t_n + \Delta t/2, (\mathbf{z}_{n+1} + \mathbf{z}_n)/2],\quad t_n = n\Delta t, \tag{27}$$

which is solved iteratively at every time step using an error tolerance, based on the L_2 norm of $w(\theta)$, given by: $\|\mathbf{w}\|_2 = \sqrt{\sum_i (w_i)^2}$. The results obtained here are based on calculations with $N = 512$ and $\Delta t = 5 \times 10^{-3}$, with a maximum error less that 10^{-5}. Calculations for $\Delta t = 5 \times 10^{-4}$ give a maximum error less that 10^{-7}. Finer meshes and lower steps were also used but showed no significant improvement of the final results, thus justifying our mesh and time step selection.

3. Results

The first subsection pertains to the linearized analysis of the initial growth/decay of a perturbation introduced at $t = t_0$. Using numerical calculations, the second subsection follows the evolution of a displacement perturbation localized about $\theta = \pi$ for different loading rates ϵ.

3.1. Linearized stability analysis

Assuming a perturbation $(\Delta v, \Delta w, \Delta\psi)$ superposed on the principal solution $(0, w_0, 0)$, the linearized perturbation equations obtained from (14) are

$$\begin{cases} \Delta\ddot v = \Delta v'' - (\mu + \lambda + w_0)\Delta v + (1 + \mu + \lambda + w_0)\Delta w' + \mu\Delta\psi, \\ \Delta\ddot w = -(1 + \mu + \lambda + w_0)\Delta v' + (\mu + w_0)\Delta w'' - (1 + \lambda)\Delta w + \mu\Delta\psi', \\ \eta\Delta\ddot\psi = \eta\Delta\psi'' - \mu(\Delta\psi - \Delta v + \Delta w'), \end{cases} \tag{28}$$

plus the initial conditions for $(\Delta v, \Delta w, \Delta\psi)$ and their time derivatives at the time of the onset of perturbation $t = t_0$.

Using the method of frozen coefficients, i.e. assuming that the rate of growth/decay of the perturbation is much higher than the

loading rate, (28) is considered as a constant coefficient equation, which admits solutions of the type

$$(\Delta v, \Delta w, \Delta\psi) = (V(k), W(k), \Psi(k)) \exp[i(\omega t + k\theta)]. \tag{29}$$

By introducing (29) into (28) and ignoring the time dependence of λ and w_0 we obtain the following dispersion equation relating ω and k

$$\det\begin{pmatrix} \mu+\lambda+w_0+k^2-\omega^2 & -ik(1+\mu+\lambda+w_0) & -\mu \\ ik(1+\mu+\lambda+w_0) & 1+\lambda+(\mu+w_0)k^2-\omega^2 & -ik\mu \\ -\mu & ik\mu & \mu+\eta(k^2-\omega^2) \end{pmatrix} = 0, \tag{30}$$

which yields the following bi-cubic polynomial in ω^2

$$\alpha_6\,\omega^6 + \alpha_4\,\omega^4 + \alpha_2\,\omega^2 + \alpha_0 = 0, \tag{31}$$

with coefficients

$$\alpha_6 \equiv \eta$$

$$\alpha_4 \equiv -\eta\left[k^2(w_0+\mu+2) + w_0 + (1+1/\eta)\mu + 2\lambda + 1\right],$$

$$\alpha_2 \equiv \eta k^4[2(w_0+\mu)+1] - k^2\{\eta[(\lambda+1)(w_0+\mu)+\lambda^2-\lambda-1] - \mu(w_0+1)\} + \eta[(\lambda+1)w_0+(\lambda+1)\mu+\lambda^2+\lambda] + (w_0+2\lambda+1)\mu,$$

$$\alpha_0 \equiv -(k^2-1)\left\{\eta k^4(w_0+\mu) - k^2\{\eta[(\lambda+1)(w_0+\mu)+\lambda^2+\lambda] - \mu w_0\} - (\lambda+1)\mu w_0 - (\lambda^2+\lambda)\mu\right\}$$

The results of (31) showing the lowest ω^2 root of (31), for $t = 0$, as a function of k for different values of the slenderness η are shown in Fig. 3(a). So, if the perturbation occurs at $t = 0$ (i.e. $w_0 = \lambda = 0$), it can be shown that (31) has three positive roots $\omega^2 \geqslant 0$ and hence, as expected, perturbation of a stress-free ring is stable. It should also be noted that for $k = 1$ the dispersion equation has a zero root $\omega^2 = 0$, reflecting the fact that $k = 1$ corresponds to a rigid body mode of the ring, easily verified since the corresponding strain measure vanishes. The group velocity $c_g \equiv d\omega/dk$ of the ring at $t = 0$ is plotted in Fig. 3(b) for a slenderness $\eta = 10^{-3}$ and in Fig. 3(c) for a slenderness $\eta = 10^{-4}$. In the last two figures all three group velocities are plotted (they correspond to the three different roots of the bicubic (31)) and represent the axial, bending and shear wave propagation speeds. It is important to notice that all of these speeds are positive for $k > 1$ and finite as $k \longrightarrow \infty$, thus justifying the choice of the Timoshenko model with rotary inertia adopted in this investigation. Observe that two roots approach the axial wave speed $c_g \longrightarrow 1$, while the third root approaches the shear wave speed, $c_g \longrightarrow \sqrt{\mu}$. As the pressure increases for $t > 0$, one of the roots of (31) becomes negative $\omega^2 < 0$ for at least a finite range of k, indicating instability of a perturbation if the range of negative roots $\omega^2 < 0$ of (31) includes an integer $k \geqslant 2$, since only finite wavenumbers make sense for the ring. The influence of dimensionless time on the minimum eigenfrequency as a function of the wavenumber is plotted in Fig. 4(a) for a fixed slenderness ($\eta = 10^{-3}$). Notice the destabilization of the ring as time progresses, as evidenced by the increasing range of wavenumbers with $\omega^2 < 0$. The influence of slenderness on the minimum eigenfrequency as a function of the wavenumber is plotted inFig. 4(b) for a fixed time ($t = 1.4$). Observe in this case the rather counterintuitive stabilizing effect of slenderness; for a given time, an increase in the slenderness parameter η – i.e. an increase of the stubbiness of the ring – increases range of wavenumbers with $\omega^2 < 0$.

The frozen coefficient analysis (study of the roots of (31)) can yield some further important information. We can find the time corresponding to the onset of a static buckling by calculating the lowest time t_b required for a zero root ω^2, which from solving $\alpha_0 = 0$ in (31) yields

$$-w_0(t_b) = (k^2-1)\eta = 3\eta, \quad (k = 2), \tag{32}$$

where in the above equation use was made of the fact that for thin elastic rings $|\lambda|, |w_0| \ll 1$. The above expression can be rewritten for the quasistatic loading case where according to (15) $w_0 \approx -\epsilon t = -\lambda$ as $\lambda = (k^2-1)\eta$ which corresponds to the buckling pressure of a quasistatically loaded ring, achieved for the lowest integer value of $k = 2$ (Brush and Almroth, 1975). For an instability to occur at the onset of buckling time t_b, we must have low loading rates $\epsilon \ll 1$, in which case inertia effects are ignored and a global buckling mode makes sense.

For finite loading rates inertia effects are important and perturbations travel at finite speeds. For such cases, failure occurs by a localized deformation mode, for which we can estimate, again from (31), another critical time t_l. Since localized deformation modes correspond to short wavelengths $k \gg 1$, the time corresponding to their onset of instability can be found by investigating the behavior of the dispersion relation (31) for large values of k, when the lowest root $\omega^2 = 0$. The corresponding critical time t_l is found by setting to zero the highest order in k (k^6 term) coefficient of α_0 in (31) which yields:

$$w_0(t_l) + \mu = 0. \tag{33}$$

Solutions of (33) using the numerical evaluation and the approximate asymptotic expression of $w_0(t)$ plus comparisons with numerical results for the onset of a localized deformation are discussed subsequently. The intercept of the dotted line in Fig. 2 with the

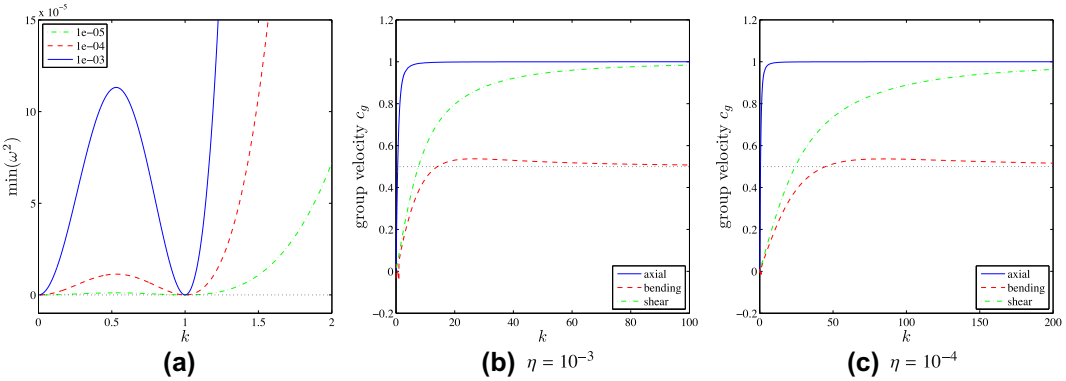

Fig. 3. (a): Effect of slenderness η on the lowest eigenfrequency ω as a function of wavenumber k at $t = 0$. (b)-(c): Group velocities c_g at $t = 0$ as a function of wavenumber k for $t = 0$ for slenderness $\eta = 10^{-3}$ and $\eta = 10^{-4}$ respectively. The thin dotted line depicts the large wave number limit for shear waves: $c_g \to \sqrt{\mu}$. Shear parameter: $\mu = 0.25$.

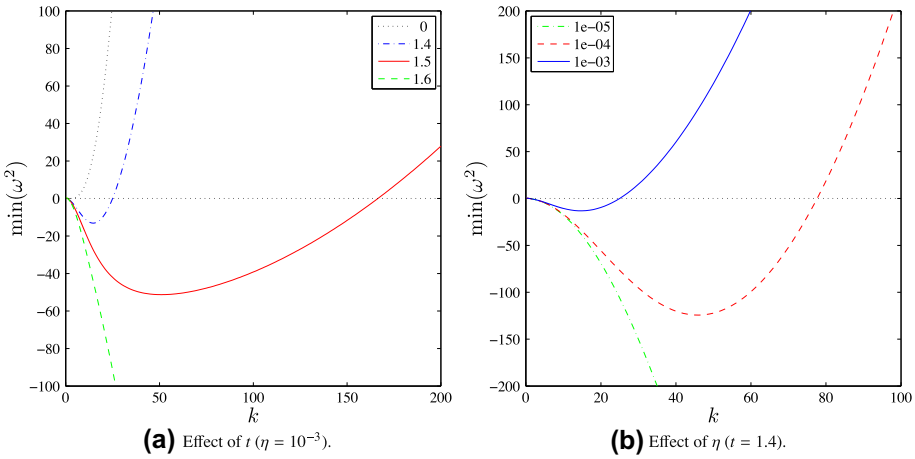

Fig. 4. (a): Lowest eigenfrequency (squared: (ω^2)) dependency on the wavenumber k for different dimensionless times t and a slenderness $\eta = 10^{-3}$. (b): Lowest eigenfrequency (squared: (ω^2)) dependency on the wavenumber k for different slenderness η at a time t = 1.4. The linearized problem's growth rates ($i\omega$) given by the roots of (31) corresponding to the frozen coefficient analysis (see Section 3.1). Shear parameter: $\mu = 0.25$, loading rate: $\epsilon = 0.5$.

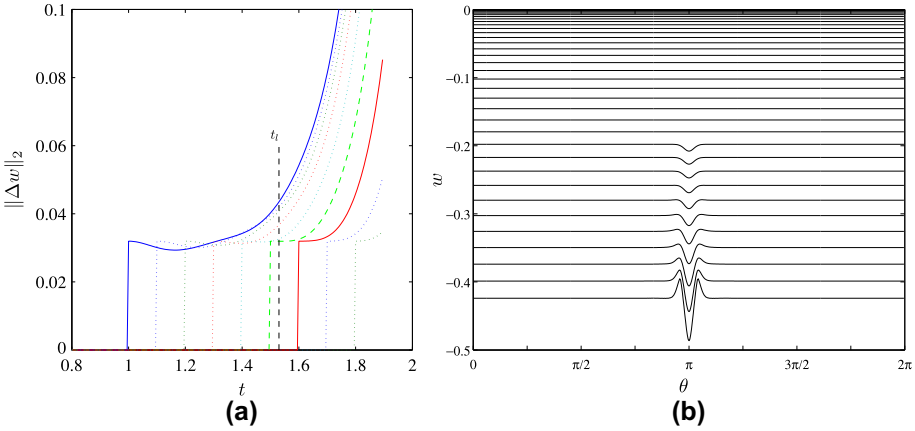

Fig. 5. (a): Influence of the time of perturbation onset on the subsequent growth of the perturbation. The vertical dashed line delimitates the localization time t_l, which for the parameter values used here is $t_l \approx 1.53$, separating stable from unstable regimes for the initial growth of an imperfection. (b): Time evolution of the radial displacement $w(\theta)$, following the introduction of a small localized perturbation at $\theta = \pi$ and at time $t_0 = 1.4$. Slenderness: $\eta = 10^{-3}$, loading rate: $\epsilon = 0.5$, shear parameter: $\mu = 0.25$, perturbation amplitude: $W_0 = 0.01$, perturbation width: $\kappa = 10$.

graphs of $w_0(t)$ gives the critical time t_l for the various loading rates ϵ.

3.2. Numerical simulations

Although we are not modeling specific experiments, the dimensionless parameters used for the numerical results presented here are motivated by the electromagnetically compressed aluminium thin rectangular section ring experiments of Mainy (2012) where: $E = 70$ GPa, $G = 26$ GPa, $\rho = 2.7 \times 10^3$ kg m^{-3}, $r = 1.5 \times 10^{-2}$ m, $h = 5 \times 10^{-4}$ m, $a = 10^{-3}$ m, $\chi = 2/3$. Correspondingly the longitudinal wave speed is: $c = \sqrt{E/\rho} \approx 5 \times 10^3$ m s^{-1}, the characteristic time: $r/c \approx 3 \times 10^{-6}$ s and the slenderness $\eta \approx 10^{-4}$. No direct comparison with the loading rate is possible between the linear pressure loading assumed in our simulations and the pulse loading resulting from the capacitor discharge in the experiments by Mainy (2012). An estimate based on the maximum velocity corresponding to the experiments for the 5 kV capacitor charge yield a dimensionless speed $\epsilon \approx 10^{-1}$ while an analogous calculation based on the calculated maximum pressure rate yield a dimensionless speed $\epsilon \approx 10^{-2}$. As a result we have selected the following values for the three dimensionless system parameters:

$$\eta = 10^{-4}, 10^{-3}; \quad \mu = 0.25; \quad \epsilon = 10^{-3}, 10^{-2}, 5 \times 10^{-1}. \tag{34}$$

In this study, the perturbation is in the form of a localized radial displacement change at $t = t_0$ centered at $\theta = \pi$

$$\begin{aligned} &\Delta v(\theta, t_0) = 0, \ \Delta w(\theta, t_0) = -W_0 \exp\left[-\kappa^2(\theta - \pi)^2\right], \ \Delta\psi(\theta, t_0) = 0, \\ &\Delta \dot{v}(\theta, t_0) = 0, \ \Delta \dot{w}(\theta, t_0) = 0, \qquad\qquad \Delta\dot{\psi}(\theta, t_0) = 0, \end{aligned} \tag{35}$$

where W_0 is the amplitude and $\kappa = 10$ is the width parameter of the rapidly decaying perturbation. All other displacement and velocity components of the initial perturbation are supposed zero. The influence of the time t_0 at the onset of perturbation and the meaning of the localization time t_l introduced in (33) is illustrated in Fig. 5 for the case of a high loading rate ($\epsilon = 0.5$) for a ring with slenderness $\eta = 10^{-3}$ and a shear parameter $\mu = 0.25$. More specifically in Fig. 5(a) we plot the norm of the perturbation $\|\Delta w\|_2 = \sqrt{\sum_i (\Delta w_i)^2}$ as a function of time for perturbations with different onset times t_0. Notice that the perturbation amplitude first

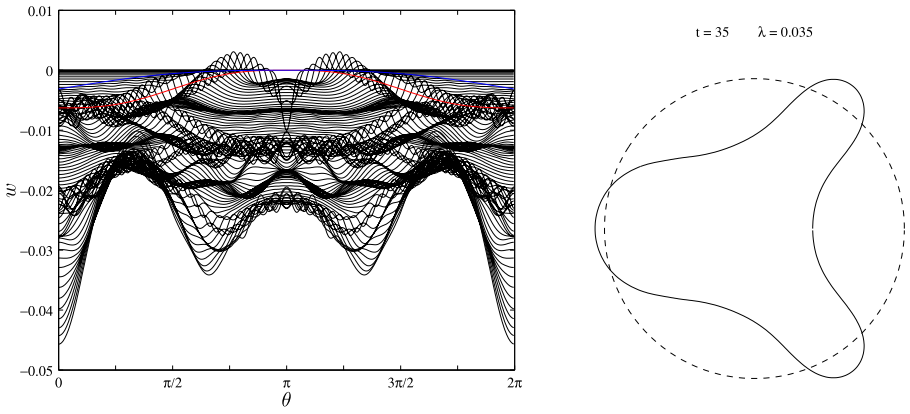

(a) $\epsilon = 0.001$

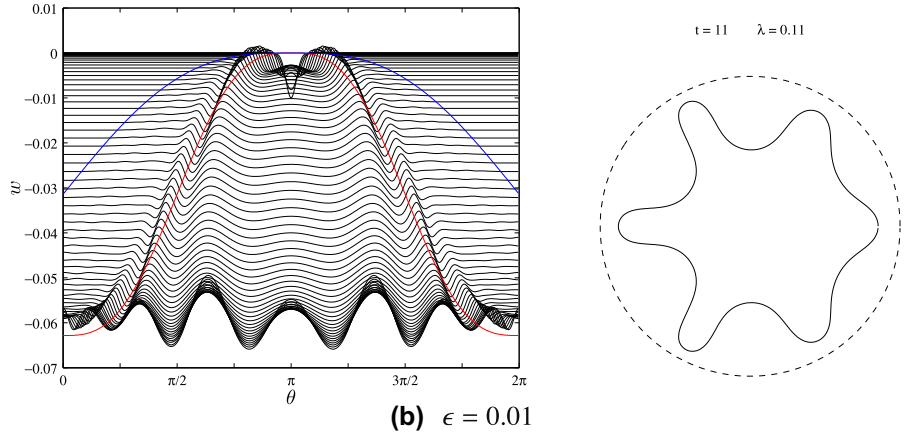

(b) $\epsilon = 0.01$

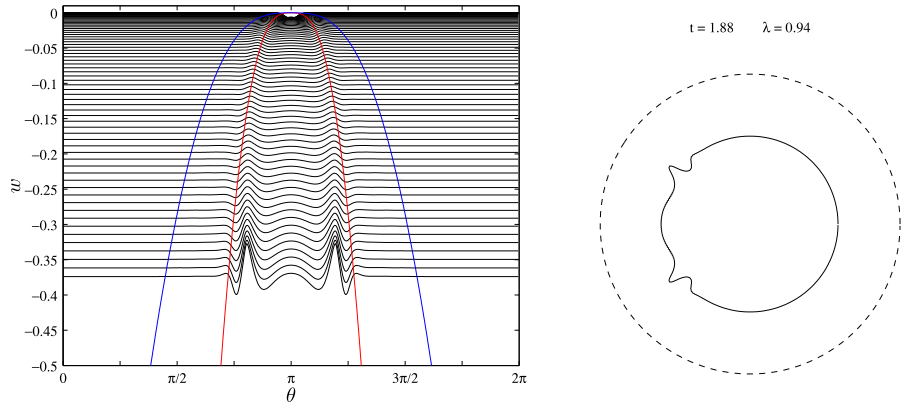

(c) $\epsilon = 0.5$

Fig. 6. Effect of the loading rate on the stability of an axially compressed ring of slenderness $\eta = 10^{-3}$ at three different loading rates (a): slow, with $\epsilon = 0.001$, (b): medium, with $\epsilon = 0.01$ and (c): high, with $\epsilon = 0.5$. In each case the left figure shows the radial displacement w as a function of θ for different times t while the right figure gives the deformed ring shape at the end of the calculation with the corresponding time and load indicated above the figure. In addition, the axial and shear wave fronts in the left figures are indicated by blue and red lines respectively. Shear parameter: $\mu = 0.25$, perturbation amplitude: $W_0 = 0.01$, perturbation width: $\kappa = 10$. (For interpretation of the references to colour in this figure legend, the reader is referred to the web version of this article.)

decreases provided that the time of perturbation onset is less $t_0 < t_l$, while the perturbation amplitude increases immediately if the perturbation occurs at a time $t_0 > t_l$.

The evolution of the radial displacement $w(\theta, t)$ for the same ring perturbed at $t_0 = 1.4$ is plotted in Fig. 5(b), which clearly shows how the maximum (in absolute value) of the radial displacement initially decays (since $t_0 < t_l$) and subsequently splits into two local maxima that propagating away from the initial perturbation location $\theta = \pi$ until the deformation localizes. This illustration of the decay/growth behavior of an initial perturbation introduced at different times t_0 for a ring under a high loading rate ($\epsilon = 0.5$) shows that the method of the frozen coefficients gives a reliable

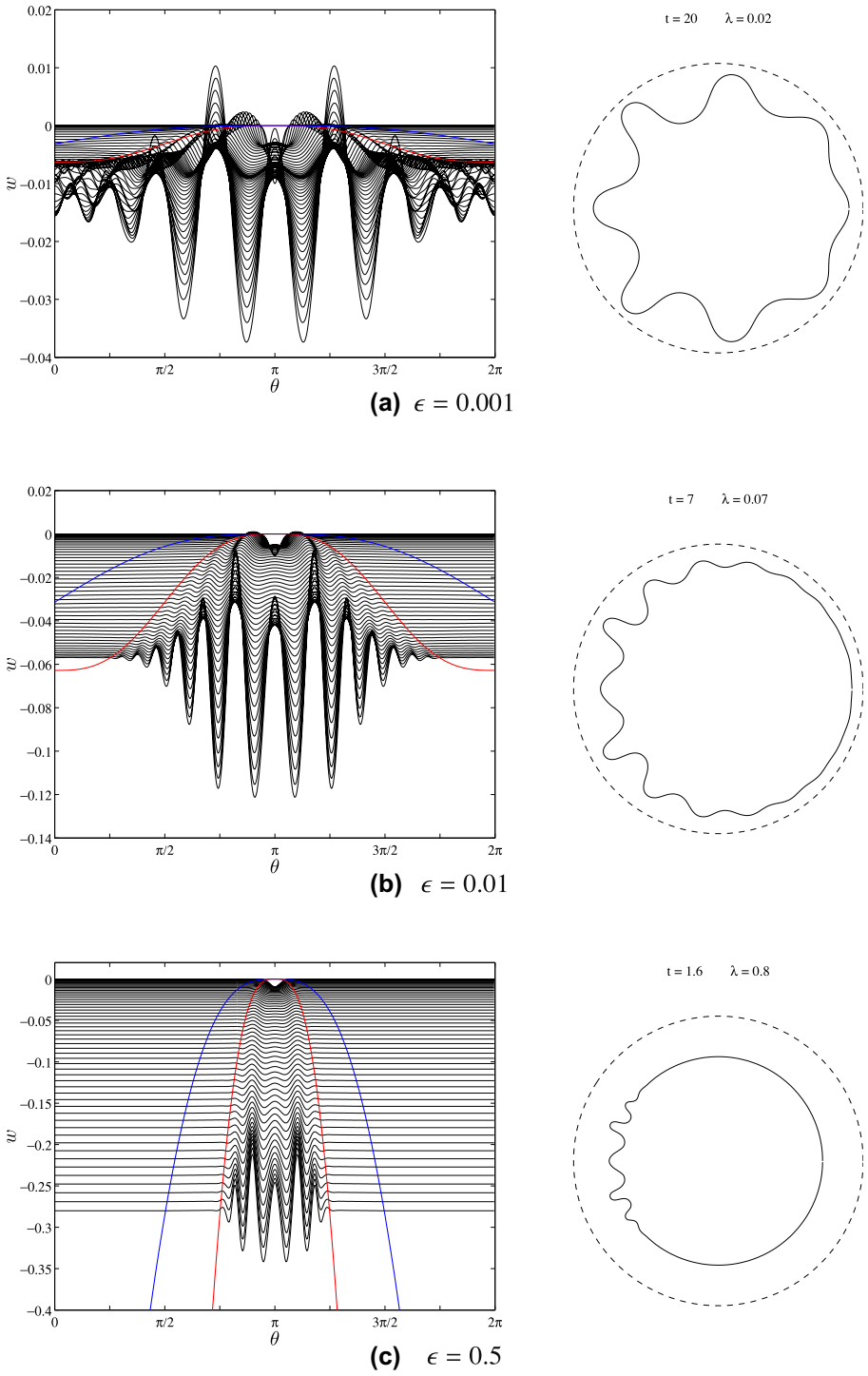

Fig. 7. Effect of the loading rate on the stability of an axially compressed ring of slenderness $\eta = 10^{-4}$ at three different loading rates (a): slow, with $\epsilon = 0.001$, (b): medium, with $\epsilon = 0.01$ and (c): high, with $\epsilon = 0.5$. In each case the left figure shows the radial displacement w as a function of θ for different times t while the right figure gives the deformed ring shape at the end of the calculation with the corresponding time and load indicated above the figure. In addition, the axial and shear wave fronts in the left figures are indicated by blue and red lines respectively. Shear parameter: $\mu = 0.25$, perturbation amplitude: $W_0 = 0.01$, perturbation width: $\kappa = 10$. (For interpretation of the references to colour in this figure legend, the reader is referred to the web version of this article.)

approximation for the characteristic time t_l separating regions of initial stability/instability for the decay/growth of a perturbation immediately following its appearance.

It is worth noticing that the time t_b at which a quasistatic buckling instability would have occurred (see discussion of (32)) is $t_b = 3\eta/\epsilon = 6 \times 10^{-3}$, well below the critical time $t_l \approx 1.53$ corresponding to this high loading rate of $\epsilon = 0.5$. As expected, a perturbation of a ring loaded at a high rate is initially stable for pressures well above the static buckling pressure, which is calculated by ignoring the speed of propagation of the perturbation. The influence of loading rate ϵ on the stability of the axially compressed ring is presented in Fig. 6 for a ring with slenderness $\eta = 10^{-3}$ (value used for the stability calculations of the previous Fig. 5) and in Fig. 7 for a ring with slenderness $\eta = 10^{-4}$ (value representing

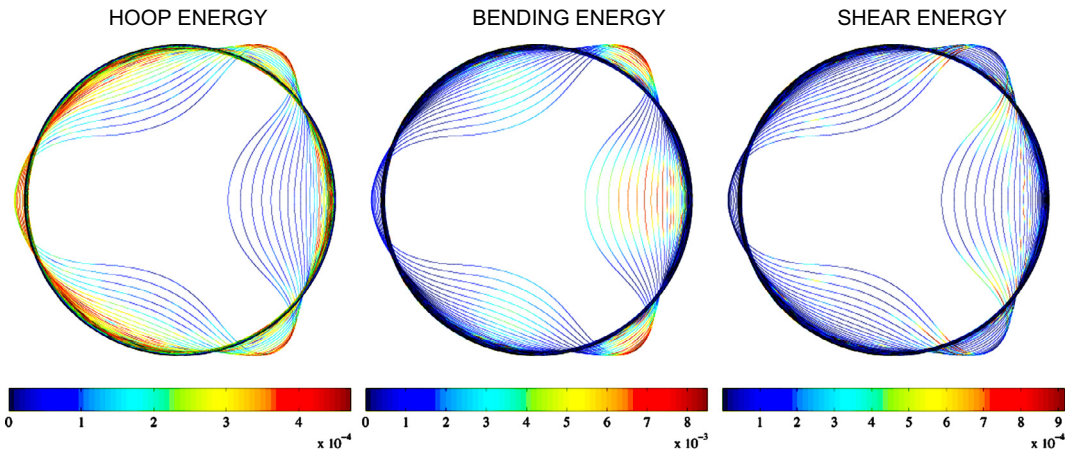

(a) Low loading rate: $\epsilon = 0.001$.

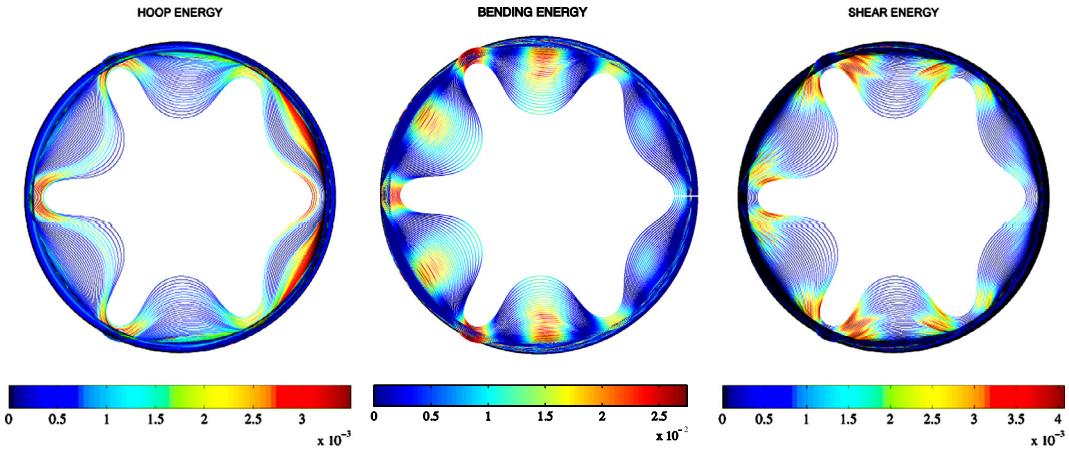

(b) Medium loading rate: $\epsilon = 0.01$.

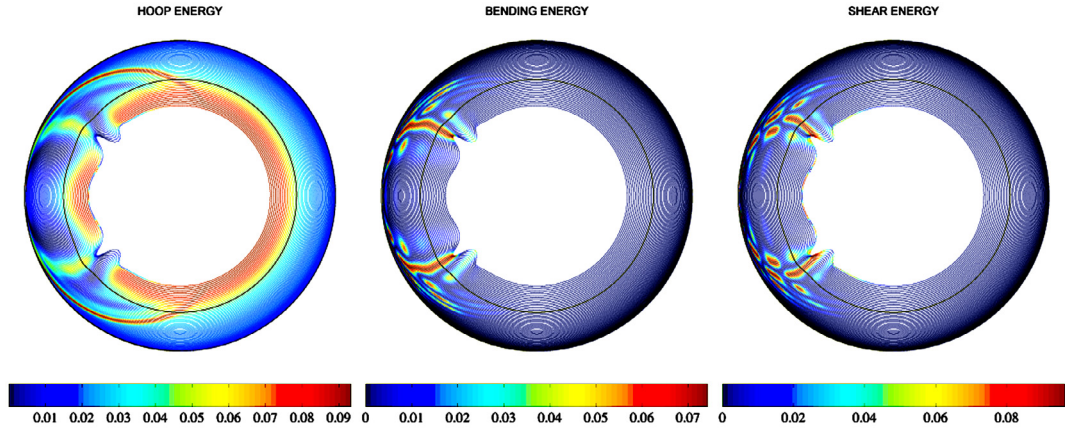

(c) High loading rate: $\epsilon = 0.5$.

Fig. 8. Local vs. global instability of the externally pressurized ring, according to the applied loading rate. The color scale refers to the value of the hoop, (axial) bending and shear elastic energy densities, respectively. (a): Evolution of deformation for an externally pressurized ring at a low loading rate $\epsilon = 0.001$. (b): Evolution of deformation for an externally pressurized ring at a medium loading rate $\epsilon = 0.01$. (c): Evolution of deformation for an externally pressurized ring at a high loading rate $\epsilon = 0.5$. The black line corresponds to the ring position at $t = t_l$. Slenderness: $\eta = 10^{-3}$, shear parameter: $\mu = 0.25$, perturbation amplitude: $W_0 = 0.01$, perturbation width: $\kappa = 10$.

the very thin rings used in the experiments by Mainy (2012)). In each figure we give results for rings subjected to three different loading rates ($\epsilon = 0.001, 0.01, 0.50$), all sharing the same shape initial perturbation (given by (35), with $W_0 = 10^{-2}$, $\kappa = 10$) and introduced at the onset of loading ($t_0 = 0$). As shown in Fig. 6 we first observe that, independently of the loading rate, the initial disturbance splits in two and generates axial (faster) and shear (slower) wavefronts propagating at speeds $c = \sqrt{E/\rho}$ and

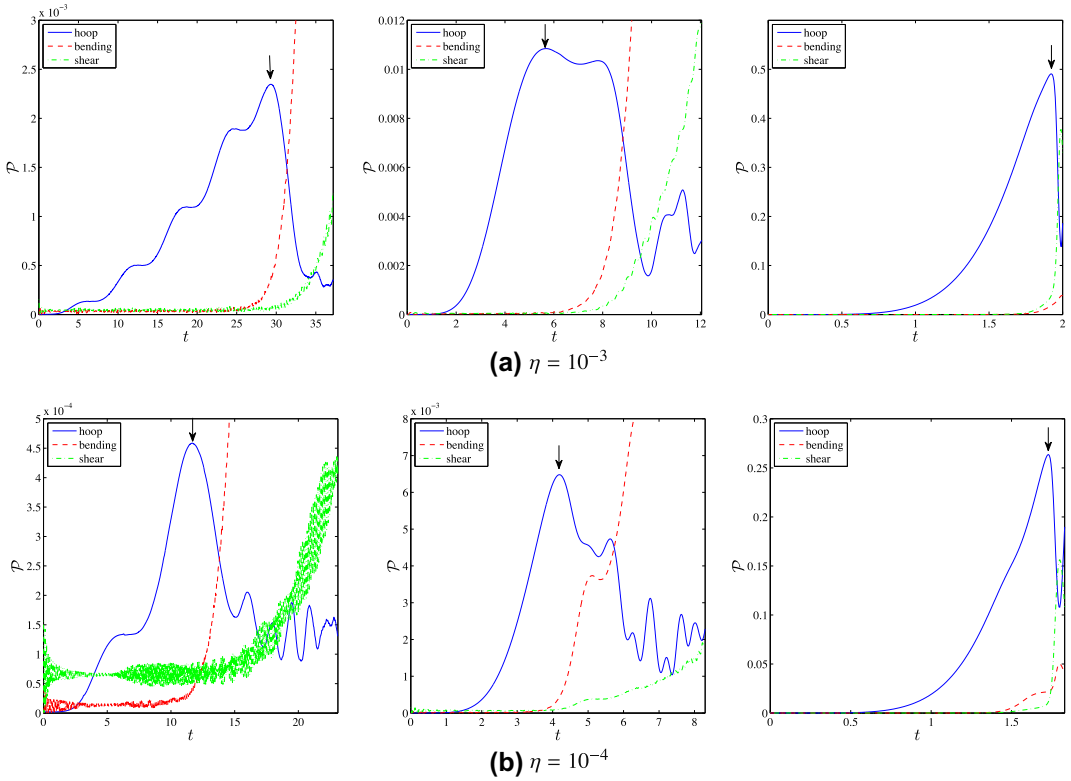

Fig. 9. Time evolution of the elastic potential energy components: axial $\mathcal{P}_a$, bending $\mathcal{P}_b$ and shear $\mathcal{P}_s$. The onset of instability is characterized by the maximum of the axial energy indicated by the black arrows. The following sharp drop of the axial energy is accompanied by a sharp increase of the bending and shear energies. In (a): Time evolution of the different internal energy components for a ring with slenderness $\eta = 10^{-3}$. In (b): Time evolution of the different internal energy components for a ring with slenderness $\eta = 10^{-4}$. Results are given for $\epsilon = 10^{-3}$ (left column) $\epsilon = 10^{-2}$ (middle column) and $\epsilon = 0.5$ (right column). Shear parameter: $\mu = 0.25$, perturbation amplitude: $W_0 = 0.01$, perturbation width: $\kappa = 10$.

$c = \sqrt{\chi G/\rho}$, respectively. At the smallest loading rate $\epsilon = 0.001$, these waves have time to travel along the entire ring circonference before triggering a global buckling mode, as seen in Fig. 6(a). On the contrary, at the highest loading rate $\epsilon = 0.5$, we observe a localization of deformation in finite time, before the disturbance has the time to travel across the entire ring as seen in Fig. 6(c). Interestingly, the disturbance propagates and grows in amplitude before it localizes in the form of a short wavelength fold whose amplitude continues to increase. At intermediate loading rates, a combination between these local and global modes of structural buckling is found to create a ring of uneven but symmetrical shape with folds of different wave lengths as seen in Fig. 6(b).

The thinnest ring response for $\eta = 10^{-4}$, as depicted in Fig. 7 is somehow different from its thicker counterpart of Fig. 6. Qualitatively the loading rate ϵ has little effect on the deformation process of the ring. The propagative phase of the disturbance is very much reduced. Instead we observe a stationary wave packet whose maximum amplitude of its envelop grows with time. What propagates in this case, at the bending wave speed, is the wave packet envelop border. Further insight regarding the dominant mode of instability of the ring and the time of its onset is provided from monitoring the different components of the elastic potential energy $\mathcal{P}_{\text{int}}$ defined in (4), respectively the axial $\mathcal{P}_a$, bending $\mathcal{P}_b$ and shear $\mathcal{P}_s$ contributions to the ring's elastic potential energy defined below

$$\mathcal{P}_a \equiv (1/2)\int_0^{2\pi} (e+\phi^2/2)^2\, d\theta, \quad \mathcal{P}_b \equiv (1/2)\int_0^{2\pi} \eta\,(\psi')^2\, d\theta,$$
$$\mathcal{P}_s \equiv (1/2)\int_0^{2\pi} \mu\,(\phi-\psi)^2\, d\theta. \tag{36}$$

The different types of instability mechanisms that appear at low and high loading rates and the relation between the onset of instability and the different components of the internal energy stored in the ring are illustrated in Fig. 8, where we present the space–time evolution of both the ring's deformed shape and the three different components of the internal energy density taken at equally spaced time intervals. At low loading rate, the elastic waves have time to travel around the ring several times and result in the global structural buckling failure mode, as seen in Fig. 8(a). Conversely, at high loading rate, the ring motion occurs over a time scale dictated by the wave propagation and result in a localized failure mode before the perturbation has the time to travel across the entire ring, as seen in Fig. 8(c). Moreover, the same figure shows that the maximum of the axial energy travels at the longitudinal wave speed whereas the maxima of bending and shear energies travel at the bending wave speed until t_l is reached. From that point on, the maxima of the bending and shear energies stop propagating and the dynamic local buckling localization occurs.

In Fig. 9, we compare the time evolution of the three components $\mathcal{P}_a, \mathcal{P}_b$ and $\mathcal{P}_s$ of the internal energy. Notice that the evolution of the axial strain energy is non-monotonic for slow loading rates but becomes monotonic as the loading rate increases, followed by a fast drop once the absolute maximum has been reached. At leading order, the increase is governed by the unperturbed radial displacement w_0, as we have $\mathcal{P}_a = \pi(w_0)^2 + \text{H.O.T.}$. The drop is monotonic at the highest loading rate and is oscillatory at lower loading rates, as seen in Fig. 9. Importantly, our numerical results show that both the local and global modes of instability are detected when $\mathcal{P}_a$ reaches its absolute maximum. We define the corresponding time as the critical time τ_c for the onset of dynamic instabilities and compare it with the previously defined onset of localization time t_l.

Regarding now the bending and transverse shear energies, they start to increase at a low rate slightly before the absolute

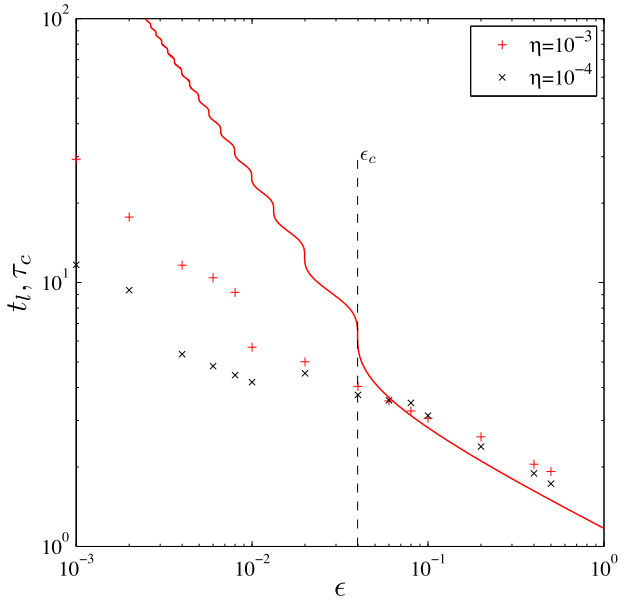

Fig. 10. Comparison of the loading rate dependence of the onset of localization time t_l, defined by Eq. (33) and the numerically calculated critical time τ_c corresponding the absolute maximum of the axial energy $\mathcal{P}_a$. The solid line represents the solution of (33) computed with the leading order asymptotic approximation (18). The critical time of maximum hoop potential energy τ_c is also computed numerically for several values of ϵ and for two different values of the slenderness: $\eta = 10^{-3}$ (points marked by $+$) and $\eta = 10^{-4}$ (points marked by $\times$). Note the good agreement between t_l and τ_c for loading rates $\epsilon > \epsilon_c$, where ϵ_c characterizes the lower bound of rates for which a localized instability mode dominates. We define the critical loading rate $\epsilon_c \approx 0.039$ (dashed line) as the loading rate above which the internal shear energy increases more rapidly than its bending counterpart. Note the discrepancy between the frozen coefficient criterion and the maximum axial energy at slow loading rate. Shear parameter: $\mu = 0.25$, perturbation amplitude: $W_0 = 0.01$, perturbation width: $\kappa = 10$.

maximum of $\mathcal{P}_a$ is attained. Then, during the phase of unstable ring deformation, the growth rate of $\mathcal{P}_b$ and $\mathcal{P}_s$ becomes large: there is an energy transfer of the axial elastic energy towards the bending and shear elastic energies. Moreover, we note that the relative increase in the bending and transverse shear energies depends on the loading rate. For small ϵ the bending energy is the first to rise sharply while at high loading rates the shear energy rises sharply ahead of the bending energy. We propose to define the loading rate at which this transition occurs as the critical loading rate ϵ_c. At low rate $\epsilon < \epsilon_c$ the structure becomes unstable via global structural (buckling type) modes for $t > \tau_c$. At high rate $\epsilon > \epsilon_c$ the structure becomes unstable via localized deformation modes for $t > \tau_c$. Finally, in Fig. 10 we show the loading rate ϵ dependence of the onset of localization time t_l, defined by Eq. (33) and of the numerically calculated critical time τ_c corresponding the absolute maximum of the axial energy $\mathcal{P}_a$. The solid line represents the solution of (33) computed with the $O(1)$ asymptotic approximation (18). The critical time for reaching the maximum hoop potential energy τ_c is also computed numerically for several values of ϵ and for two different values of the slenderness: $\eta = 10^{-3}$ (points marked by $+$) and $\eta = 10^{-4}$ (points marked by $\times$). Note the good agreement between t_l and τ_c for loading rates $\epsilon > \epsilon_c$, where ϵ_c characterizes rates for which a localized instability mode dominates and their divergence for loading rates $\epsilon < \epsilon_c$.

4. Conclusion

As a model structure to study the influence of inertia and loading rates on the stability of a structure that becomes unstable even at static loads (structures with buckling modes), we study an elastic ring subjected to external hydrostatic pressure applied at different rates ϵ (appropriately non-dimensionalized with respect to elastic axial wave speed). Unlike existing analyses of this phenomenon that are based on modal analysis to find the fastest growth rate – a method that is only meaningful for slow loading rates in view of characteristic wave speeds present in the structure – the ring's stability is studied by following the evolution of a localized small perturbation. It is shown that for small values of the applied loading rate the structure fails through a global (buckling-type) deformation mode, while for large values of the applied loading rate the structure fails by a localized mode of deformation. The term "*failure*" is being used rather loosely in this paper to describe the dramatic departure from the uniform deformation pattern of the ring and not its destruction.

Using a frozen coefficient analysis to approximate the instantaneous dispersion relation of traveling perturbations, we have defined analytically an onset of localization time t_l that determines when a localized mode of instability can occur in the structure as time evolves. A more detailed study of the numerical calculations shows that the onset of an instability is triggered when the maximum of the axial energy is reached at a numerically calculated time τ_c; for global (buckling type) modes bending energy dominates and the bending energy increases faster than the shear energy as the instability progresses. The situation is reversed for localized type modes of instability, where shear energy increases much more rapidly than its bending counterpart. The critical loading rate at which this crossover occurs ϵ_c is found numerically. An important result of this work is that the analytically obtained localization time t_l is a very good estimate of the onset of instability time τ_c for loading rates $\epsilon > \epsilon_c$.

The approach used in the present study is based on spatially localized initial perturbations of the structure. The obvious question to ask is what would the response be in the case of equivalent initial imperfections, as for example in the work by Budiansky and Hutchinson (1964), which is motivated by the quasistatic case. Preliminary calculations by Wen and Triantafyllidis (2013) show the same qualitative response, i.e. same critical times for the onset of instability but different final deformation patterns when the same geometrically localized mode is used either as initial perturbation or as initial imperfection in the rapidly loaded ring problem.

This work presents a new approach for investigating the dynamic stability of structures that exhibit instabilities even under static loadings. Since real-life structures of engineering interest exhibit plasticity, the next step in this work is to apply the ideas introduced here to elastoplastic structures. Eventually the influence of different types of dynamic loading (i.e. step, pulse) need to be considered as well as a more realistic modeling of the electromagnetic loading conditions, investigation that are currently under way to complete this work.

Acknowledgements

This work of Dr. Thibaut Putelat has been funded through a post-doctoral fellowship by the École Polytechnique. The authors express their gratitude to Prof. K. Ravi-Chandar, of the Aerospace Engineering and Engineering Mechanics Department at the University of Texas at Austin for many stimulating discussions while on sabbatical leave at the Solid Mechanics Laboratory of the École Polytechnique during the Academic Year 2011–2012, made possible by the generosity of the CNRS and the École Polytechnique. Prof. N. Triantafyllidis also acknowledges partial support from the National Science Foundation under Grant DMI 0400143.

References

Amabili, M., Paidoussis, M., 2003. Review of studies on geometrically nonlinear vibrations and dynamics of circular cylindrical shells and panels, with and without fluid–structure interaction. Appl. Mech. Rev. 56, 349–381.

Anderson, D., Lindberg, H.E., 1968a. Dynamic pulse buckling of cylindrical shells under transient lateral pressures. AIAA J. 6, 589–598.
Anderson, D.L., Lindberg, H.E., 1968b. Dynamic pulse buckling of cylindrical shells under transient lateral pressures. AIAA J., 459–472.
Boresi, A., Reichenbach, H., 1967. Energy methods in parametric excitation of rings. Nucl. Eng. Des.
Brush, D., Almroth, B., 1975. Buckling of Bars, Plates, and Shells. McGraw-Hill I.
Budiansky, B., Hutchinson, J., 1964. Dynamic buckling of imperfection sensitive structures. Proceedings XI International Congress of Applied Mechanics, Munich.
Carrier, G., 1945. On the vibrations of the rotating ring. Q. Appl. Math. 3, 235–245.
Dempsey, K., 1996. Dynamic nonlinear forcing of elastic rings. Proc. R. Soc. London Ser. A, 1927–1943.
Florence, A., 1968. Buckling of viscoplastic cylindrical shells due to impulsive loading. AIAA J. 6, 532–537.
Goodier, J., McIvor, I., 1964. The elastic cylindrical shell under nearly uniform radial pressure. J. Appl. Mech., 259–266.
Gourdin, W., 1989. Analysis and assessment of electromagnetic ring expansion at a high-strain-rate test. J. Appl. Phys. 65, 411.
Graff, K., 1971. On dispersion of elastic waves in rings. Int. J. Mech. Sci. 13, 107–111.
Graff, K.F., 1975. Wave Motion in Elastic Solids. Oxford University Press.
Hesthaven, J., Gottlieb, S., Gottlieb, D., 2007. Spectral methods for time-dependent problems. Cambridge Monographs on Applied and Computational Mathematics, vol. 21. Cambridge University Press.
Jones, N., Okawa, D.M., 1976. Dynamic plastic buckling of rings and cylindrical shells. Nucl. Eng. Des., 125–147.
Koning, C., Taub, J., 1933. Impact buckling of thin bars in the elastic range hinged at both ends. Luftfahrtfosrchung 10, 55–64.
Lindberg, H., 1964. Buckling of a very thin cylindrical shell due to an impulsive pressure. J. Appl. Mech., 267–272.
Lindberg, H., 1974. Stress amplification in a ring caused by dynamic instability. J. Appl. Mech., 392–400.
Lindberg, H., Florence, A., 1987. Dynamic Pulse Buckling. Martinus Nijhoff Publishers.
Mainy, A., 2012. Dynamic buckling of thin metallic rings under external pressure. Master's thesis, University of Texas.
Mercier, S., Molinari, A., 2003. Predictions of bifurcation and instabilities during dynamic extension. Int. J. Solids Struct. 40 (8), 1995–2016.
Morley, S., 1961. Elastic wave in a naturally curved rod. Q. J. Mech. Appl. Math. 14, 155–172.
Shenoy, V., Freund, L., 1999. Necking bifurcations during high strain rate extension. J. Mech. Phys. Solids 47 (11), 2209–2233.
Simitses, G.J., Hodges, D.H., 2006. Fundamentals of Structural Stability. Elsevier.
Simmonds, J., 1979. Accurate nonlinear equations and a perturbation solution for the free vibrations of a circular elastic ring. J. Appl. Mech. 46, 156–160.
Sorensen, N., Freund, L., 2000. Unstable neck formation in a ductile ring subjected to impulsive radial loading. Int. J. Solids Struct. 37 (16), 2265–2283.
Triantafyllidis, N., Waldenmyer, J., 2004. Onset of necking in electro-magnetically formed rings. J. Mech. Phys. Solids 52, 2127–2148.
Wah, T., 1970. Dynamic buckling of thin circular rings. Int. J. Mech. Sci. 12, 143–155.
Weideman, J., Reddy, S., 2000. A MATLAB differentiation matrix suite. ACM Trans. Math. Softw. 26, 465–519.
Wen, G. and Triantafyllidis, N. 2013. (in preparation).
Zhang, H., Ravi-Chandar, K., 2006. On the dynamics of necking and fragmentation – I. Real-time and post-mortem observations in al 6061-O. Int. J. Fract. 142, 183–217.
Zhang, H., Ravi-Chandar, K., 2008. On the dynamics of necking and fragmentation—II. Effect of material properties, geometrical constraints and absolute size. Int. J. Fract. 150, 3–36.